Supplement of Earth Syst. Dynam., 13, 231–249, 2022
https://doi.org/10.5194/esd-13-231-2022-supplement

Earth System Dynamics
Open Access

Supplement of

Weakened impact of the Atlantic Niño on the future equatorial Atlantic and Guinea Coast rainfall

Koffi Worou et al.

Correspondence to: Koffi Worou (koffi.worou@uclouvain.be)

Supplement

S1 Supplement figures

Figure S1. SST indices of the Atlantic Niño: JAS mean of monthly SST anomalies averaged over the Atlantic Niño area, for the 1985–2014 period (green curves). The linear (blue curves) and quadratic (orange curves) trends are superimposed on each panel. SST outputs from CMIP6 historical simulations (30 GCMs) and the ERA5 reanalysis are considered.

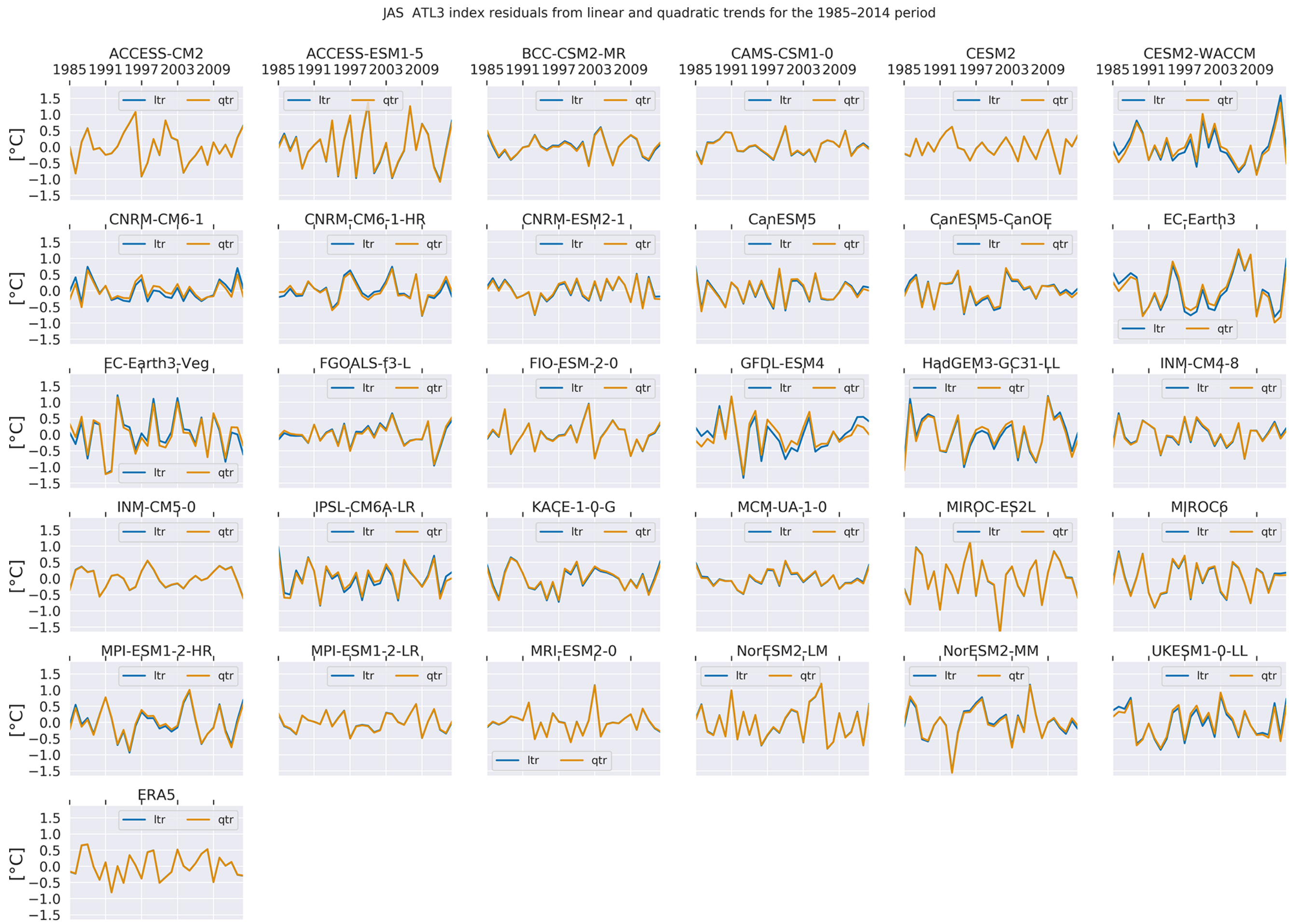

Figure S2. Residuals of the detrended JAS ATL3 SST indices after removing the linear trend (blue curves) and the quadratic trend (orange curves). The displayed 1985–2014 time series are from 30 CMIP6 models and ERA5.

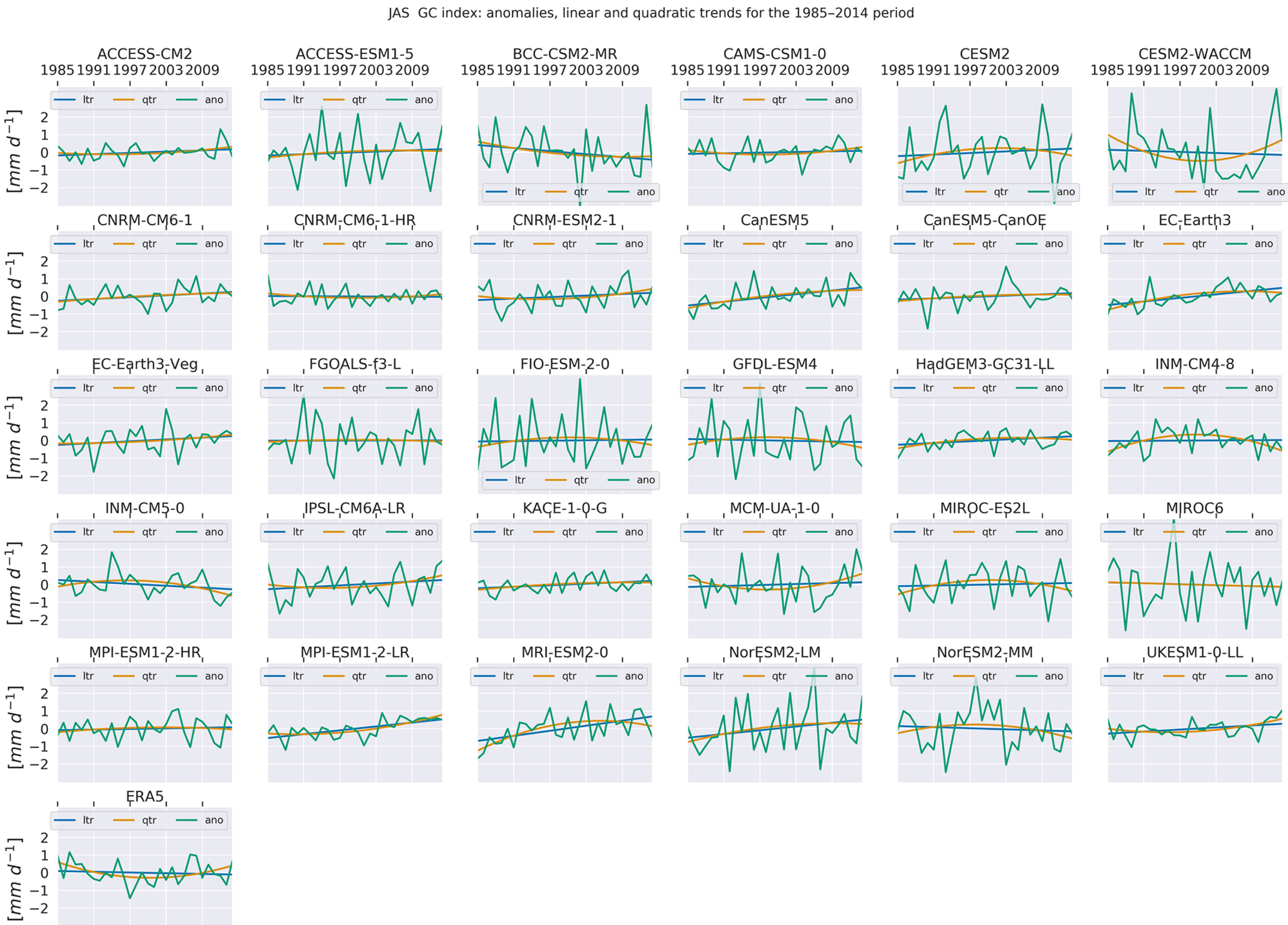

Figure S3. JAS mean of monthly rainfall anomalies averaged over the Guinea Coast, for the 1985–2014 period (green curves). The linear (blue curves) and quadratic (orange curves) trends are superimposed on each panel. Rainfall outputs from CMIP6 historical simulations (30 GCMs) and the ERA5 reanalysis are considered.

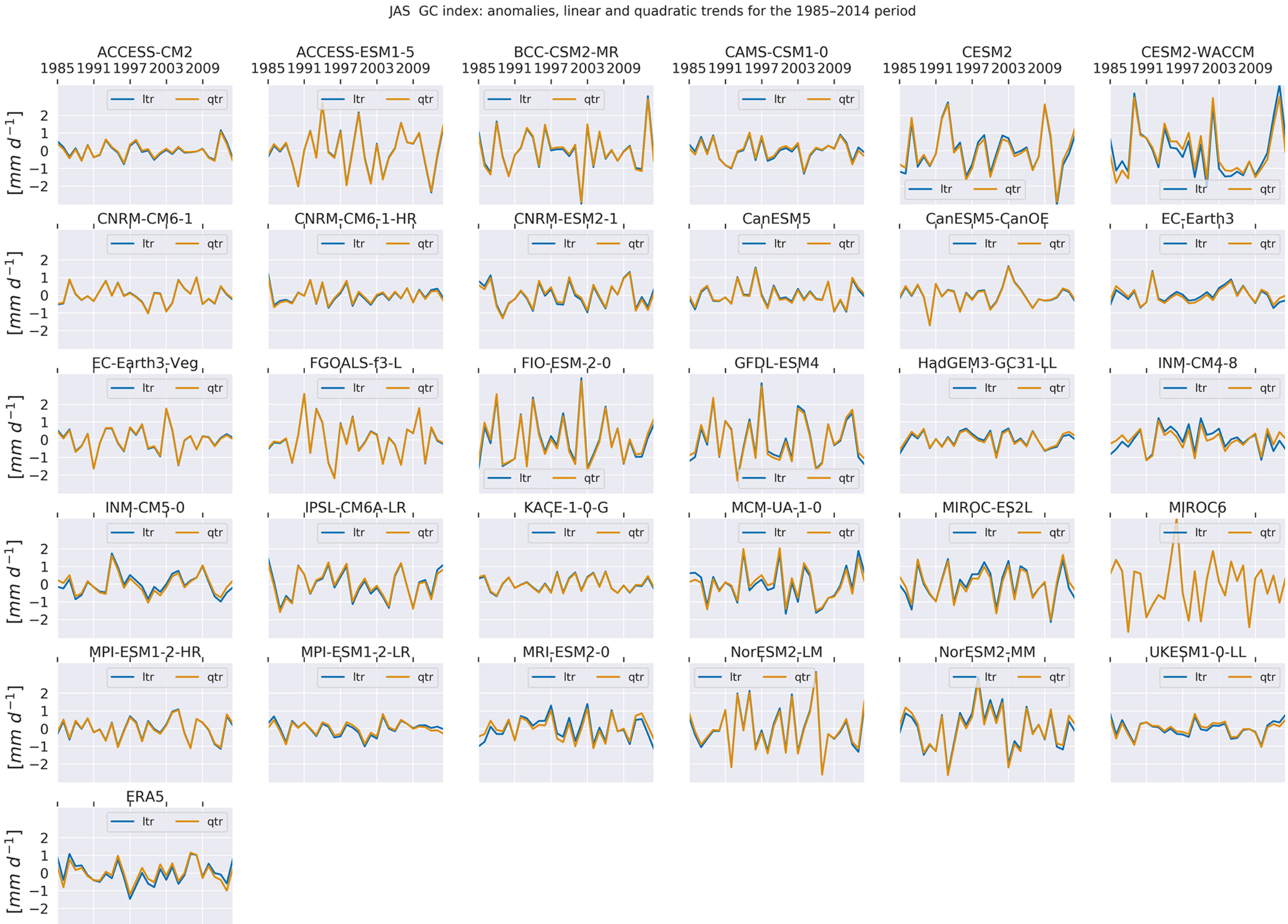

Figure S4. Residuals of the detrended JAS Guinea Coast rainfall indices after removing the linear trend (blue curves) and the quadratic trend (orange curves). The displayed 1985–2014 time series are from 30 CMIP6 models and ERA5.

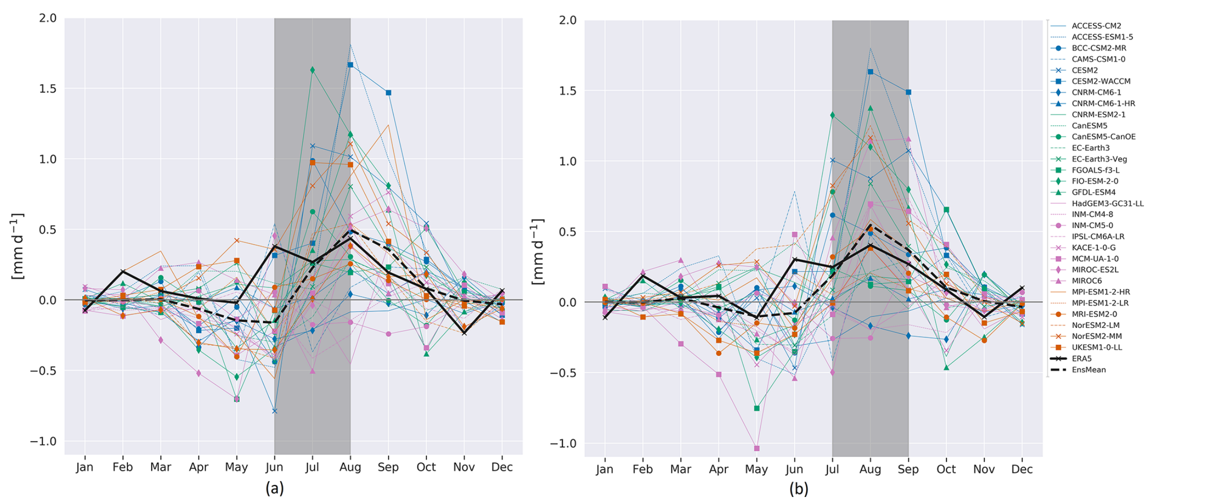

Figure S5. Monthly rainfall anomalies of Guinea Coast regressed onto the JJA **(a)** and JAS **(b)** standardized ATL3 SST index over the 1985–2014 period. Outputs from 30 CMIP6 historical simulations and ERA5 are analyzed. Gray vertical bands indicate the SST season considered in each case.

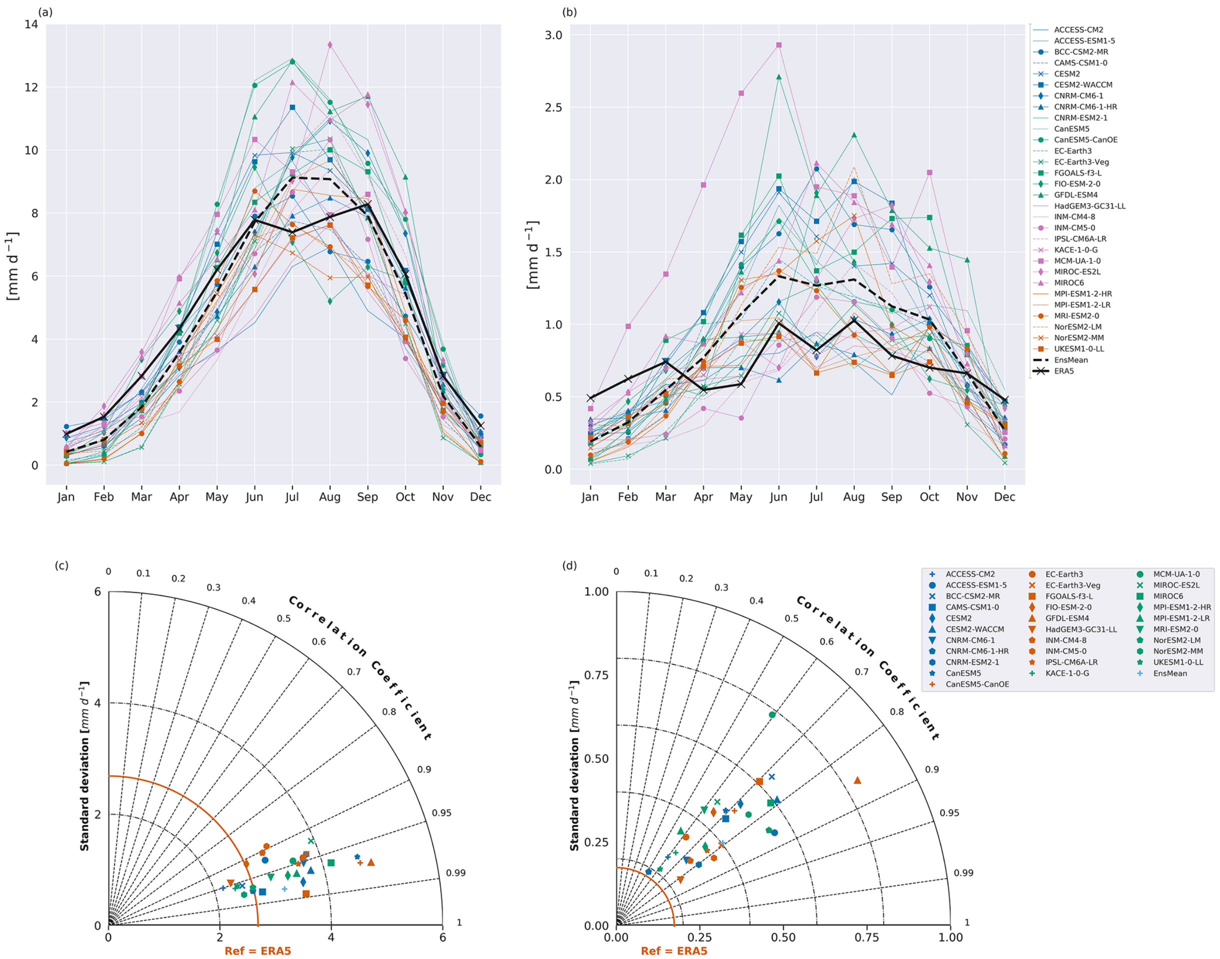

Figure S6. Annual cycle of the **(a)** rainfall intensity and **(b)** rainfall standard deviation in Guinea Coast. In **(a)** and **(b)**, thick lines represent the annual cycle of the multimodel ensemble mean (dashed line) and ERA5 (black line marked with a cross). The other lines represent the annual cycle in each of the 30 GCMs. Taylor diagram of the **(c)** rainfall annual cycle, and **(d)** rainfall standard deviation annual cycle in the GCB area, where ERA5 is chosen as the reference. The annual cycle is computed for the 1985–2014 period.

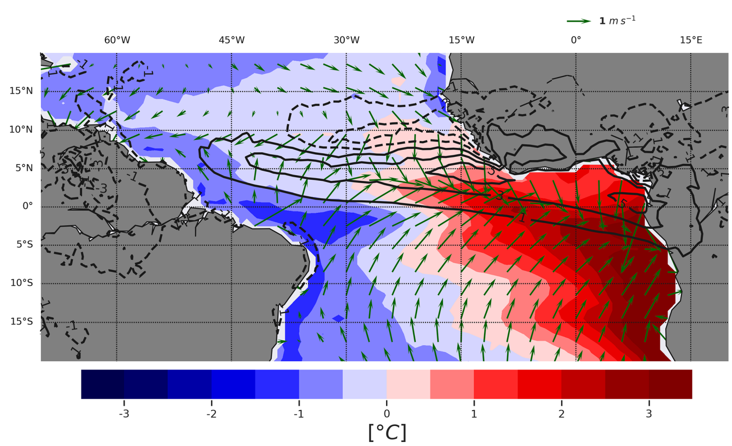

Figure S7. Mean biases (relative to ERA5) of the ensemble mean of 22 GCMs for the JAS SST (in colors), rainfall (in contours) and 10 m horizontal wind (arrows) over 1985–2014. Among the 30 GCMs used in this study, these 22 models correspond to the ones that have the 10 m horizontal wind components for both the historical and SSP5–8.5 simulations.

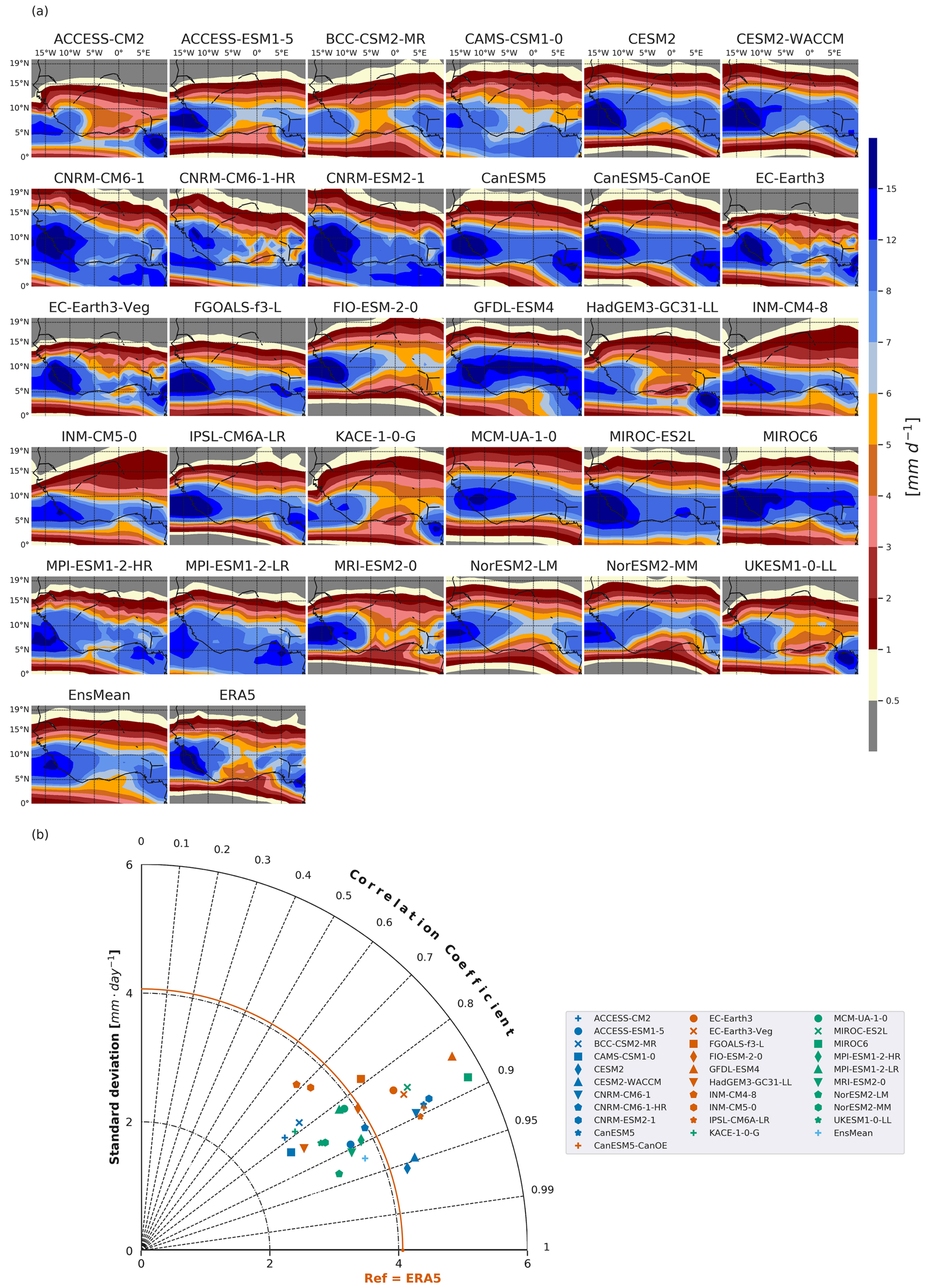

Figure S8. **(a)** 1985–2014 JAS rainfall mean in 30 GCMs and in ERA5. **(b)** Taylor diagram of the JAS rainfall mean over West Africa (4–20° N), where the mean JAS rainfall spatial distributions in the models are compared to the one in ERA5.

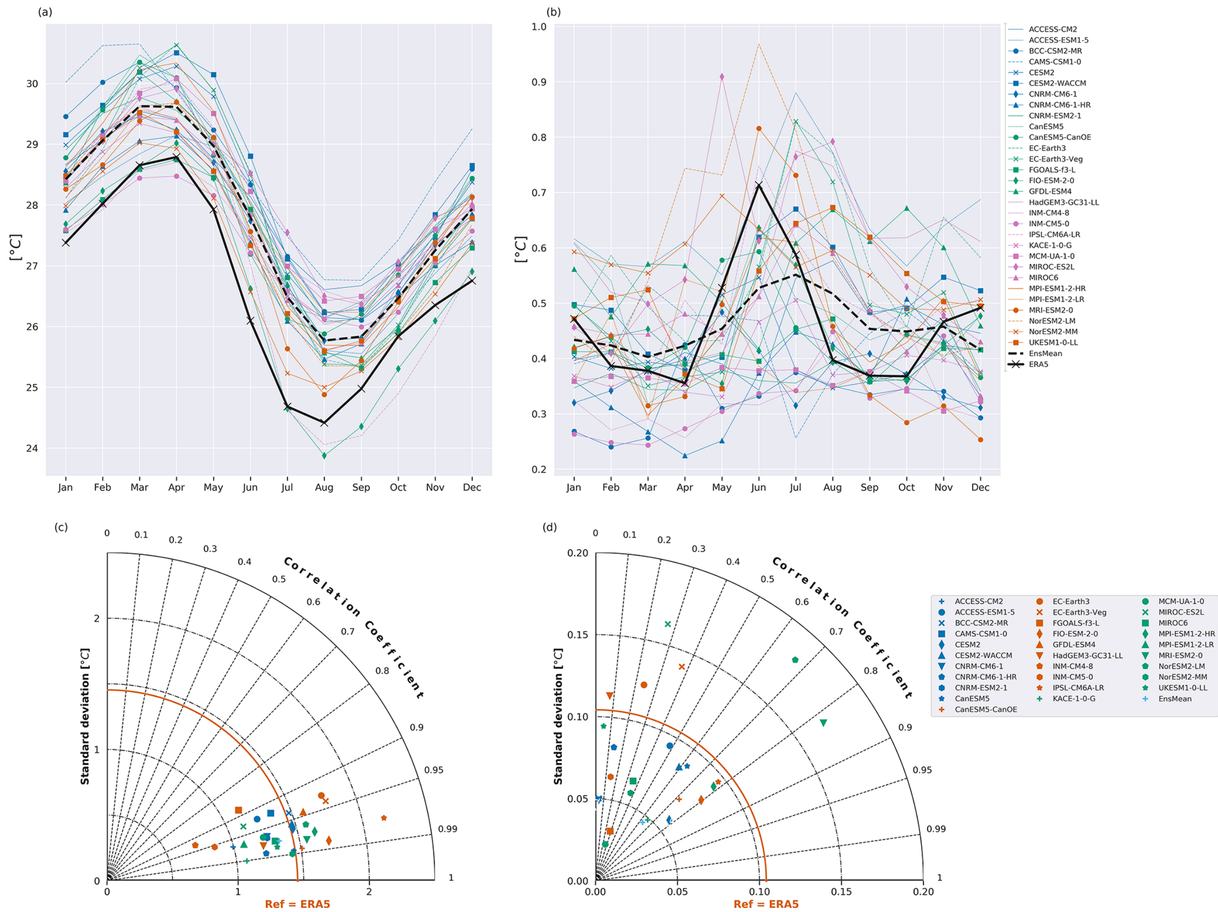

Figure S9. Annual cycle of the **(a)** sea surface temperature and **(b)** sea surface temperature standard deviation in the ATL3 area. In **(a)** and **(b)**, thick lines represent the annual cycle of the multimodel ensemble mean (dashed line) and ERA5 (black line marked with a cross). The other lines represent the annual cycle in each of the 30 GCMs. Taylor diagram of the **(c)** SST annual cycle and **(d)** SST standard deviation annual cycle in the ATL3 area, where ERA5 is chosen as the reference. The annual cycle is computed for the 1985–2014 period.

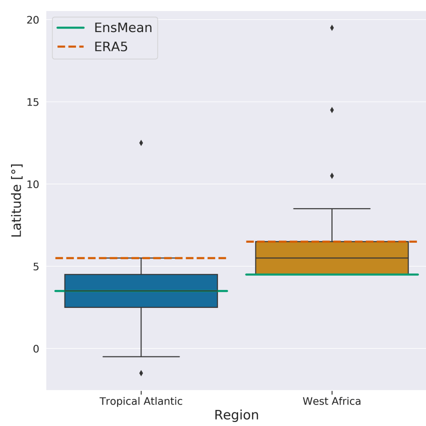

Figure S10. Position in latitude of the maximum JAS rainfall associated with the JAS ATL3 SST index in the tropical Atlantic (zonal average over 70° W and 10° E, blue boxplot) and West Africa (zonal average between 20° W and 10° E, dark gold boxplot). The boxplots represent the distribution of the positions computed in each of the 30 models. The black line inside each box represents the median value of the models, and the outliers are represented by the diamond-shaped symbols. The other horizontal lines represent the mean positions obtained in the multi-model ensemble mean (green line) and ERA5 (dashed orange line).

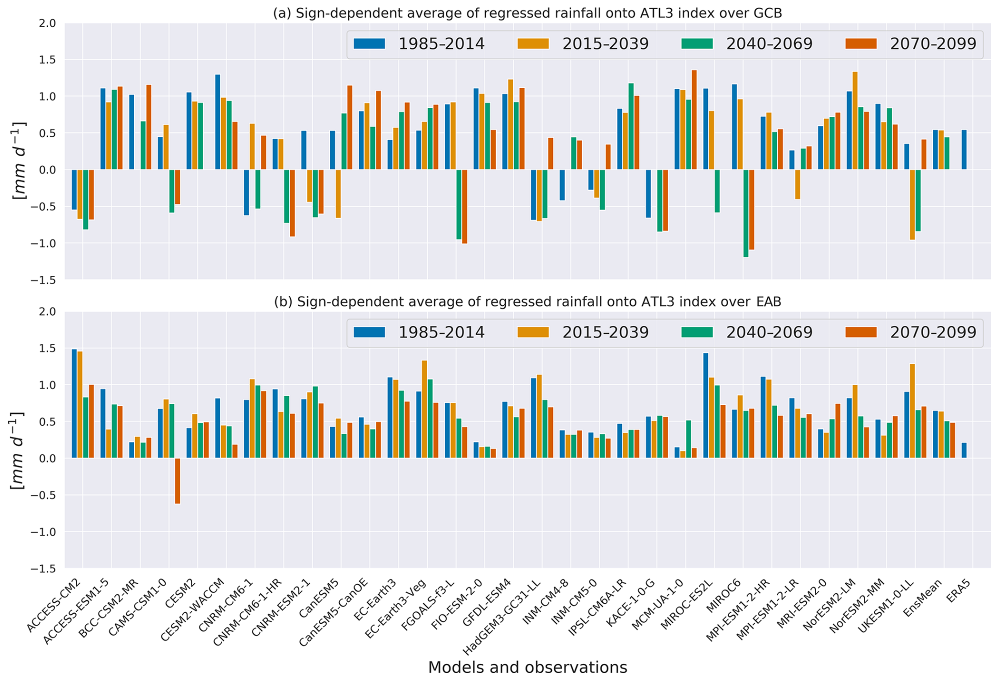

Figure S11. Sign-dependent average of the JAS rainfall regressed coefficients onto the standardized JAS ATL3 SST index over the Guinea Coast box **(a)** and the equatorial Atlantic box **(b)** for the 30 GCMs over the present-day, near-term, mid-term and long-term periods. The sign-dependent average value in ERA5 is computed for the 1985–2014 period.

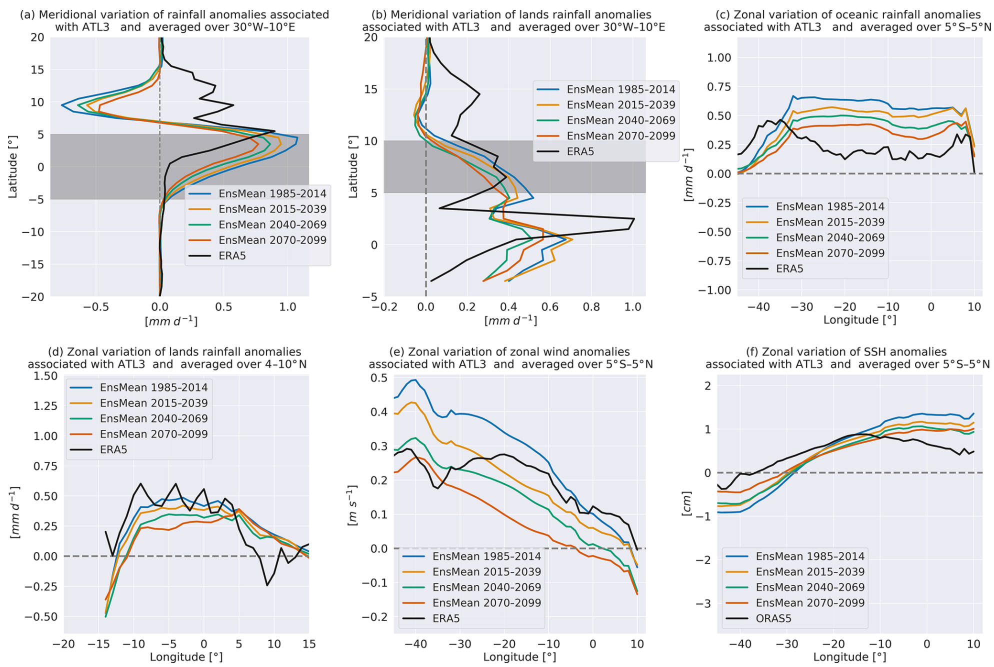

Figure S12. Rainfall anomalies associated with the standardized JAS ATL3 SST index and averaged over 30° W and 10° E for oceanic areas **(a)** and land areas **(b)**. Gray bands in **(a)** and **(b)** represent the equatorial Atlantic and Guinea Coast regions, respectively. Zonal variation of the JAS rainfall anomalies associated with the standardized JAS ATL3 SST index and averaged over the equatorial Atlantic **(c)** and Guinea Coast regions **(d)**. Zonal variation of the JAS 850 hPa zonal wind **(e)** and sea surface height anomalies **(f)** associated with the standardized JAS ATL3 SST index and averaged over the equatorial Atlantic. In each panel, the solid black line represents ERA5 or ORAS5 for 1985–2014, and the other solid lines represent the ensemble mean of the 30 GCMs for the present and future periods.

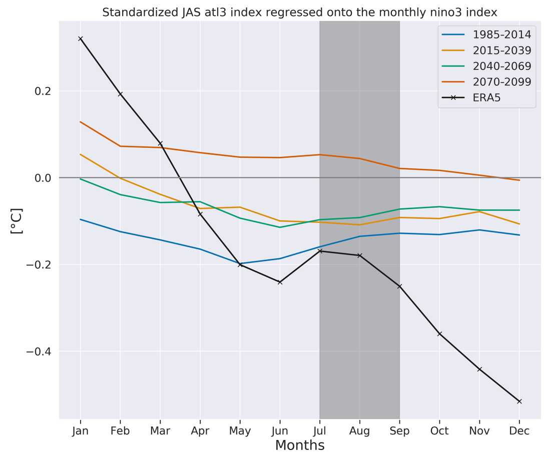

Figure S13. Monthly stratified Niño3 index regressed onto the standardized JAS ATL3 SST index for different periods. The 1985–2014 period is considered for ERA5 (black curve). The other curves correspond to the ensemble mean response of 30 CMIP6 models over four different periods: 1985–2014, 2015–2039, 2040–2069 and 2070–2099.

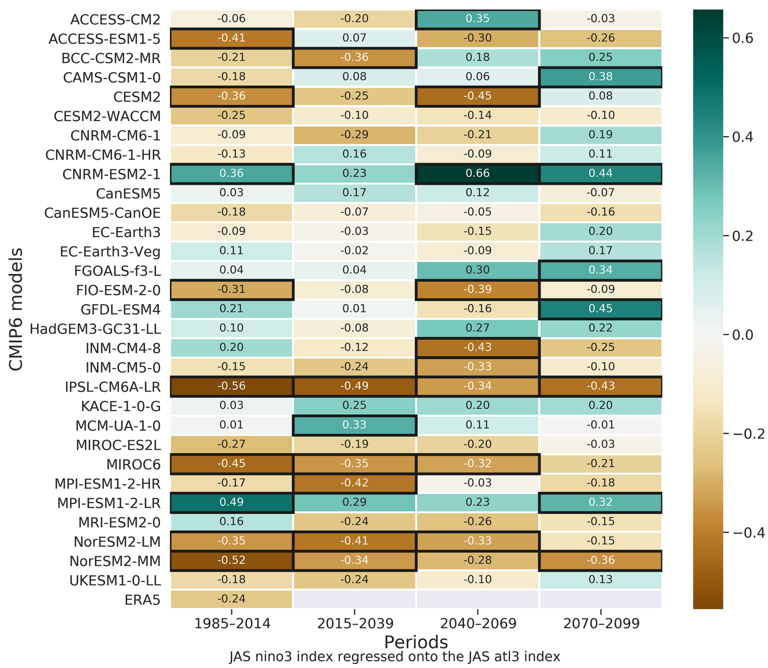

Figure S14. JAS Niño3 index correlation with the JAS ATL3 SST index over four different periods. 30 CMIP6 models and the reanalysis ERA5 are analyzed. Significant regression coefficients at 90 % confidence level (Student test) are highlighted with a black box.

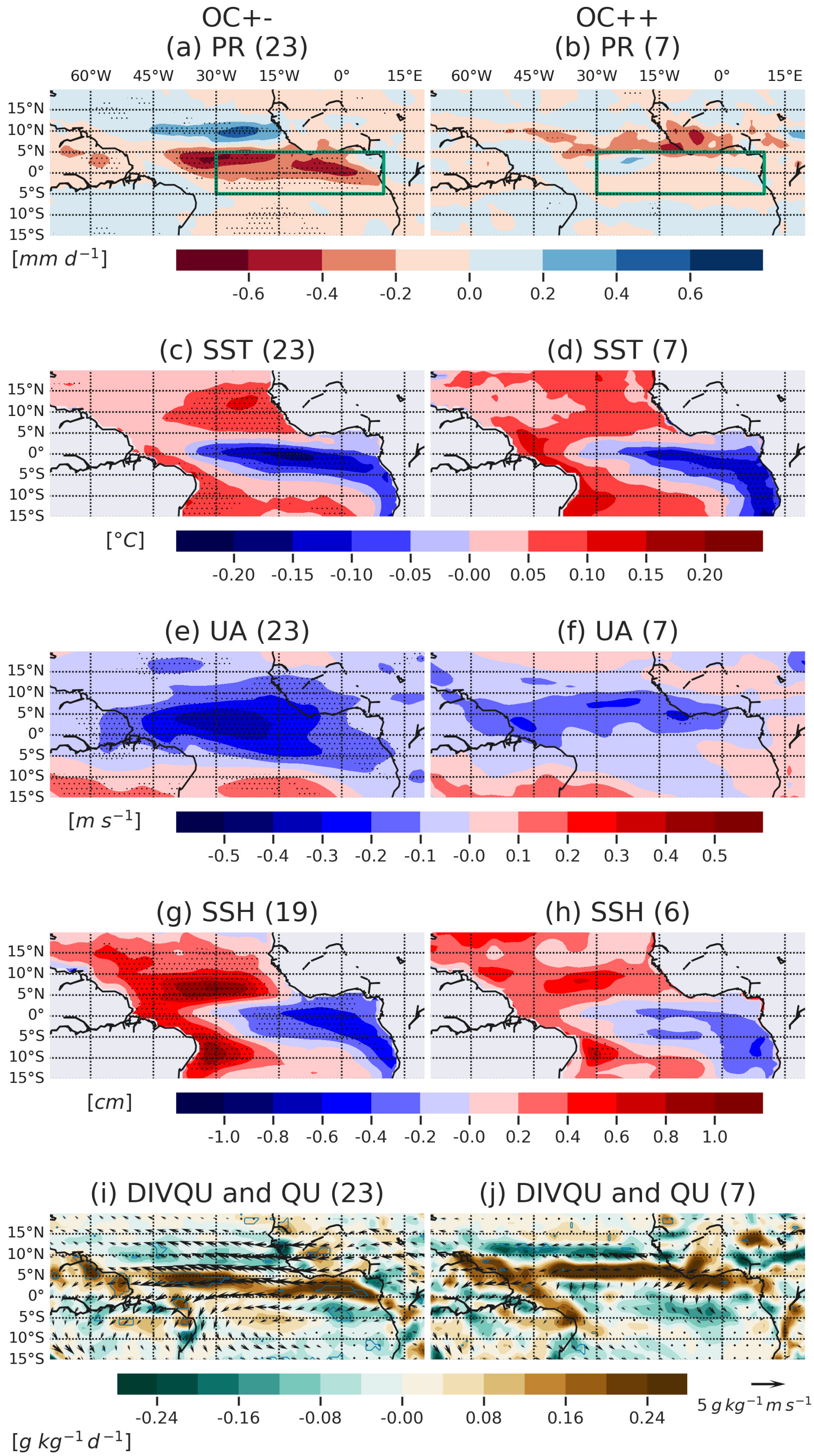

Figure S15. Long-term changes of the JAS rainfall **(a, b)**, SST **(c, d)**, 850 hPa zonal wind **(e, f)**, sea surface height **(g, h)**, moisture flux (vectors) and moisture flux divergence (in colors) **(i, j)** regression patterns associated with the standardized JAS ATL3 SST index, relative to the present-day climate (2070–2099 minus 1985–2014). Stippling in **(a)**–**(h)** and contours in **(i)**–**(j)** indicate areas where the mean change (in colors) is significant at 95 % level according to a two-sided Welch t-test and where at least two thirds of the models agree on the sign of the change. The number of models in each group is indicated in parentheses.

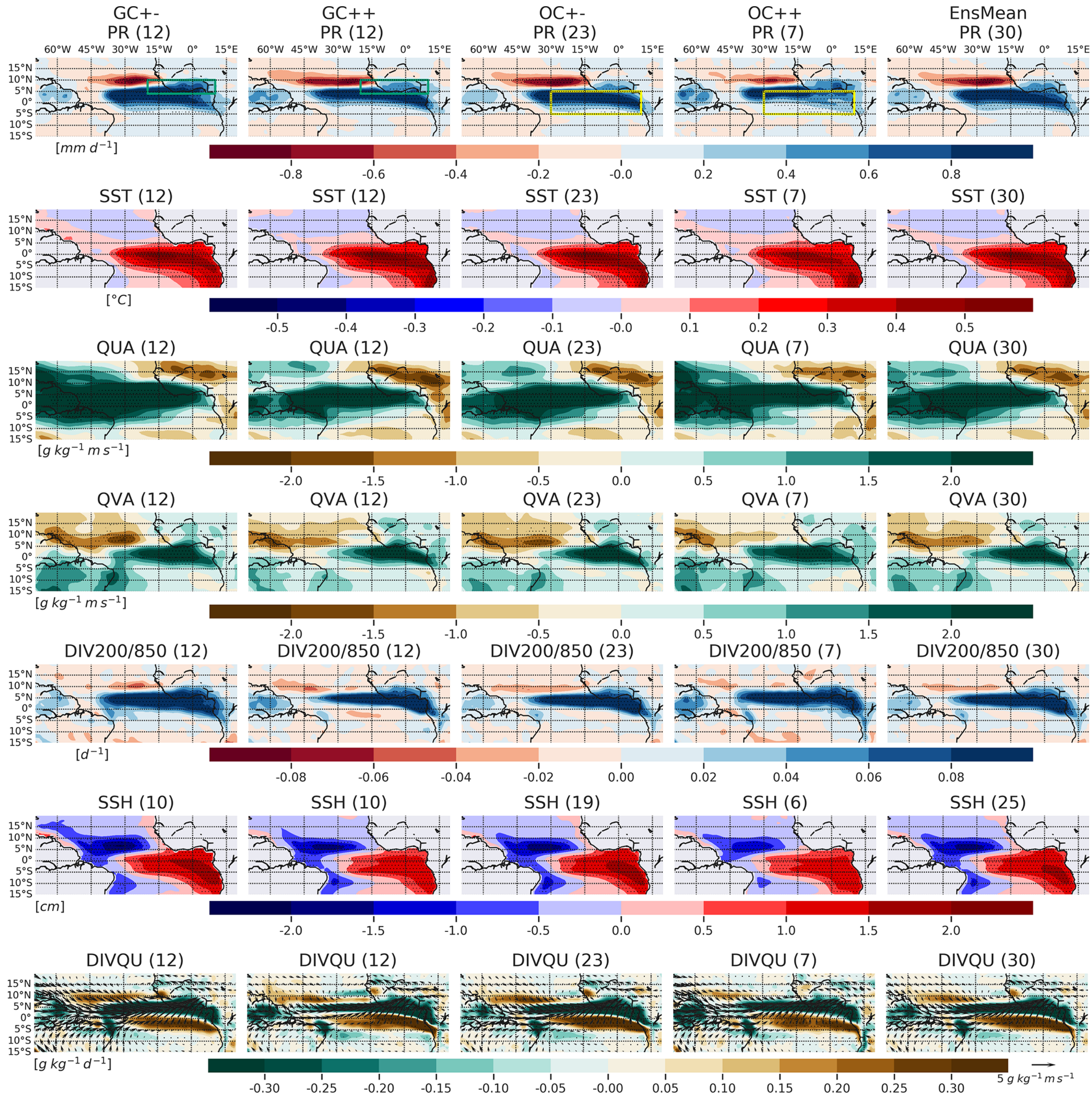

Figure S16. 1985–2014 regression maps of the JAS rainfall, SST, 850 hPa zonal and meridional moisture flux, DIV200/850, SSH, 850 hPa moisture flux and moisture flux divergence anomalies onto the standardized JAS ATL3 SST index, for the GC+−, GC++, OC+−, OC++ and the 30 GCMs EnsMean groups. Stippling indicates areas where the regression coefficients are significant at 95 % confidence level for at least 50 % of the models in each group, and where more than 80 % of the models agree on the sign of the regression coefficient. The number of models in each group is indicated in parentheses.

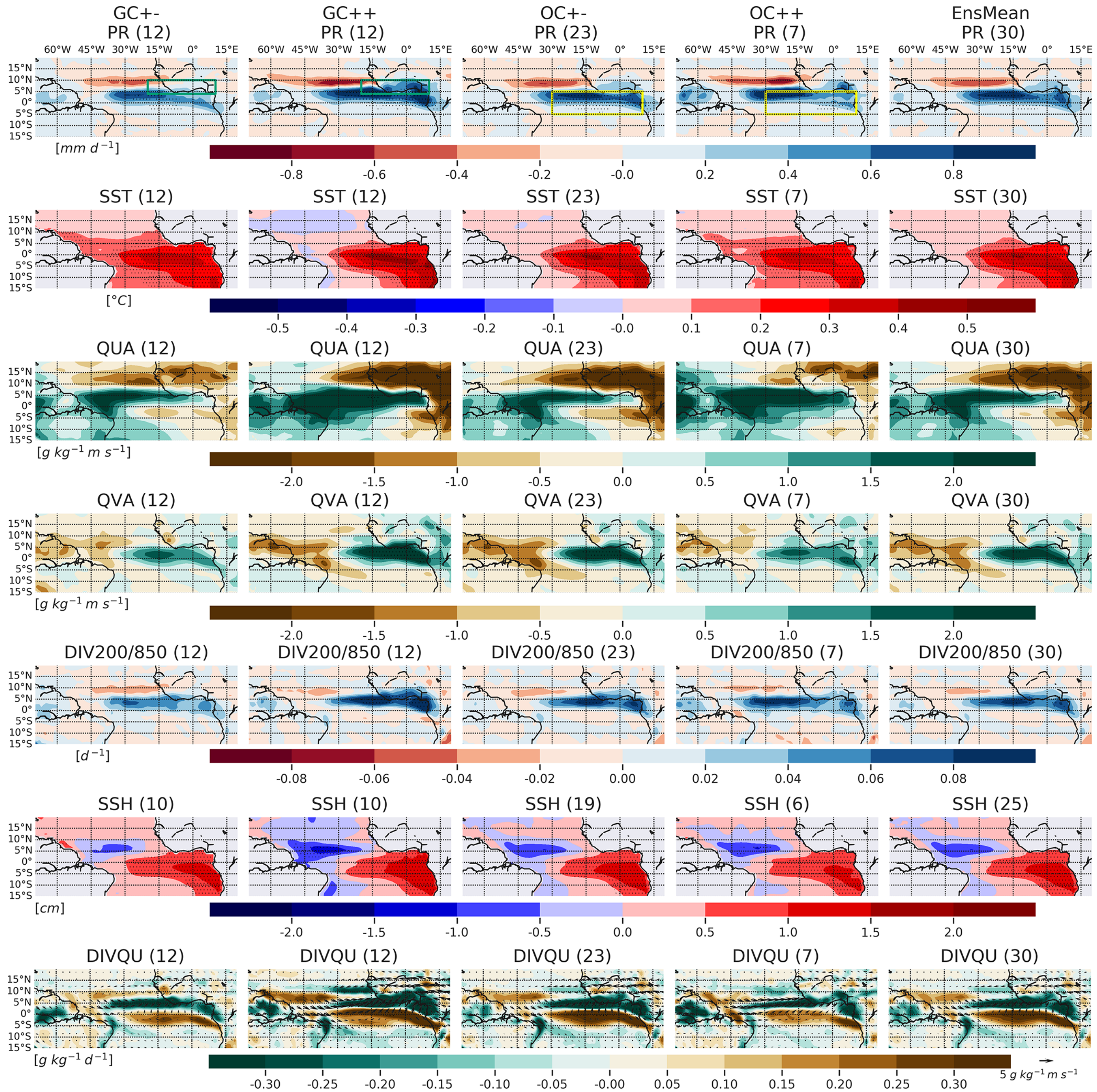

Figure S17. 2070–2099 regression maps of the JAS rainfall, SST, 850 hPa zonal and meridional moisture flux, DIV200/850, SSH, 850 hPa moisture flux and moisture flux divergence anomalies onto the standardized JAS ATL3 SST index, for the GC+−, GC++, OC+−, OC++ and the 30 GCMs EnsMean groups. Stippling indicates areas where the regression coefficients are significant at 95 % confidence level for at least 50 % of the models in each group, and where more than 80 % of the models agree on the sign of the regression coefficient. The number of models in each group is indicated in parentheses.

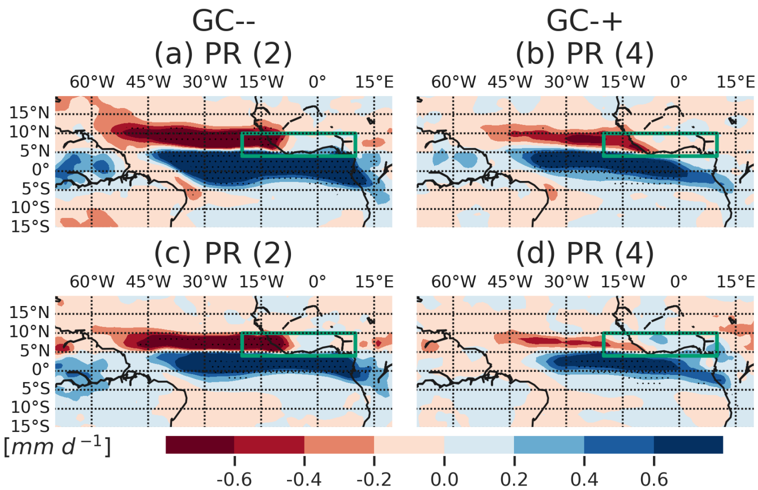

Figure S18. 1985–2014 **(a, b)** and 2070–2099 **(c, d)** regression maps of the JAS rainfall anomalies onto the standardized JAS ATL3 SST index for the GC−− **(a, c)** and GC−+ **(b, d)** groups. Stippling indicates areas where the regression coefficients are significant at 95 % confidence level for at least 50 % of the models in each group, and where more than 80 % of the models agree on the sign of the regression coefficient. The number of models in each group is indicated in parentheses.

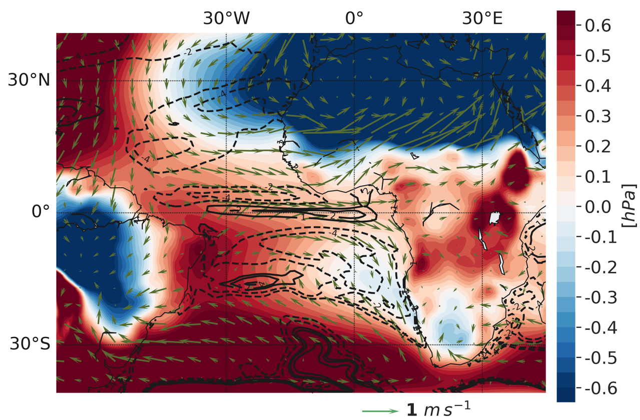

Figure S19. Long-term mean state change (2070–2099 minus 1985–2014) of the sea level pressure (in colors), 10 m horizontal wind (arrows) and mixed layer depth (in contours in m). These changes are computed for the JAS season and averaged over 22 GCMs (Table 1).

S2 Supplement tables

Table S1. Multi-model averages of the JAS Guinea Coast rainfall, EAB rainfall, EAB SST, EAB 850 hPa zonal wind, EAB DIV200/850 and EAB SSH anomalies related to the JAS EAM in the GC++, GC+− and Ensmean groups.

		GC++	GC+−	EnsMean	Unit
GCR	1985–2014	0.40	0.56	0.37	$mm\,d^{-1}$
	2070–2099	0.49	0.10	0.24	$mm\,d^{-1}$
	% of change	22.63	−83.01	−34.81	
OCR	1985–2014	0.55	0.67	0.62	$mm\,d^{-1}$
	2070–2099	0.42	0.33	0.40	$mm\,d^{-1}$
	% of change	−22.93	−50.74	−35.95	
SST	1985–2014	0.33	0.33	0.33	°C
	2070–2099	0.28	0.26	0.27	°C
	% of change	−15.22	−20.68	−18.50	
UA	1985–2014	0.22	0.31	0.24	$m\,s^{-1}$
	2070–2099	0.12	0.03	0.05	$m\,s^{-1}$
	% of change	−44.18	−89.74	−79.44	
DIV200/850	1985–2014	0.04	0.06	0.05	d^{-1}
	2070–2099	0.03	0.02	0.03	d^{-1}
	% of change	−32.88	−61.60	−49.81	
ZOS	1985–2014	0.75	1.02	0.87	cm
	2070–2099	0.68	0.73	0.66	cm
	% of change	−9.40	−28.46	−23.42	

Table S2. Models in the different categories for the 2015–2039 period.

GC++	GC+−	GC−+	GC−−	OC+	OC−
CAMS-CSM1-0	ACCESS-ESM1-5	CNRM-CM6-1	ACCESS-CM2	BCC-CSM2-MR	ACCESS-CM2
CanESM5-CanOE	BCC-CSM2-MR	INM-CM4-8	HadGEM3-GC31-LL	CAMS-CSM1-0	ACCESS-ESM1-5
EC-Earth3	CESM2	KACE-1-0-G	INM-CM5-0	CESM2	CESM2-WACCM
EC-Earth3-Veg	CESM2-WACCM			CNRM-CM6-1	CNRM-CM6-1-HR
FGOALS-f3-L	CNRM-CM6-1-HR			CNRM-ESM2-1	CanESM5-CanOE
GFDL-ESM4	CNRM-ESM2-1			CanESM5	EC-Earth3
MPI-ESM1-2-HR	CanESM5			EC-Earth3-Veg	FGOALS-f3-L
MRI-ESM2-0	FIO-ESM-2-0			HadGEM3-GC31-LL	FIO-ESM-2-0
NorESM2-LM	IPSL-CM6A-LR			MIROC6	GFDL-ESM4
	MCM-UA-1-0			NorESM2-LM	INM-CM4-8
	MIROC-ES2L			UKESM1-0-LL	INM-CM5-0
	MIROC6				IPSL-CM6A-LR
	MPI-ESM1-2-LR				KACE-1-0-G
	NorESM2-MM				MCM-UA-1-0
	UKESM1-0-LL				MIROC-ES2L
					MPI-ESM1-2-HR
					MPI-ESM1-2-LR
					MRI-ESM2-0
				NorESM2-MM	

Table S3. Models in the different categories for the 2040–2069 period.

GC++	GC+−	GC−+	GC−−	OC+	OC−
CanESM5	ACCESS-ESM1-5	CNRM-CM6-1	ACCESS-CM2	CAMS-CSM1-0	ACCESS-CM2
EC-Earth3	BCC-CSM2-MR	HadGEM3-GC31-LL	INM-CM5-0	CESM2	ACCESS-ESM1-5
EC-Earth3-Veg	CAMS-CSM1-0	INM-CM4-8	KACE-1-0-G	CNRM-CM6-1	BCC-CSM2-MR
IPSL-CM6A-LR	CESM2			CNRM-ESM2-1	CESM2-WACCM
MPI-ESM1-2-LR	CESM2-WACCM			EC-Earth3-Veg	CNRM-CM6-1-HR
MRI-ESM2-0	CNRM-CM6-1-HR			KACE-1-0-G	CanESM5
	CNRM-ESM2-1			MCM-UA-1-0	CanESM5-CanOE
	CanESM5-CanOE			MRI-ESM2-0	EC-Earth3
	FGOALS-f3-L				FGOALS-f3-L
	FIO-ESM-2-0				FIO-ESM-2-0
	GFDL-ESM4				GFDL-ESM4
	MCM-UA-1-0				HadGEM3-GC31-LL
	MIROC-ES2L				INM-CM4-8
	MIROC6				INM-CM5-0
	MPI-ESM1-2-HR				IPSL-CM6A-LR
	NorESM2-LM				MIROC-ES2L
	NorESM2-MM				MIROC6
	UKESM1-0-LL				MPI-ESM1-2-HR
					MPI-ESM1-2-LR
					NorESM2-LM
					NorESM2-MM
					UKESM1-0-LL

Table S4. Models in the different categories for the 2070–2099 period.

GC++	GC+−	GC−+	GC−−	OC+	OC−
ACCESS-ESM1-5	CAMS-CSM1-0	CNRM-CM6-1	ACCESS-CM2	BCC-CSM2-MR	ACCESS-CM2
BCC-CSM2-MR	CESM2	HadGEM3-GC31-LL	KACE-1-0-G	CESM2	ACCESS-ESM1-5
CanESM5	CESM2-WACCM	INM-CM4-8		CNRM-CM6-1	CAMS-CSM1-0
CanESM5-CanOE	CNRM-CM6-1-HR	INM-CM5-0		CanESM5	CESM2-WACCM
EC-Earth3	CNRM-ESM2-1			MIROC6	CNRM-CM6-1-HR
EC-Earth3-Veg	FGOALS-f3-L			MRI-ESM2-0	CNRM-ESM2-1
GFDL-ESM4	FIO-ESM-2-0			NorESM2-MM	CanESM5-CanOE
IPSL-CM6A-LR	MIROC-ES2L				EC-Earth3
MCM-UA-1-0	MIROC6				EC-Earth3-Veg
MPI-ESM1-2-LR	MPI-ESM1-2-HR				FGOALS-f3-L
MRI-ESM2-0	NorESM2-LM				FIO-ESM-2-0
UKESM1-0-LL	NorESM2-MM				GFDL-ESM4
					HadGEM3-GC31-LL
					INM-CM4-8
					INM-CM5-0
					IPSL-CM6A-LR
					KACE-1-0-G
					MCM-UA-1-0
					MIROC-ES2L
					MPI-ESM1-2-HR
					MPI-ESM1-2-LR
					NorESM2-LM
					UKESM1-0-LL